NANO LETTERS
Letter
Cite This: Nano Lett. 2018, 18, 4247−4256
pubs.acs.org/NanoLett

Three-Dimensional High-Entropy Alloy−Polymer Composite Nanolattices That Overcome the Strength−Recoverability Trade-off

Xuan Zhang,[†] Jiahao Yao,*[,‡] Bin Liu,[†] Jun Yan,[§] Lei Lu,[‡] Yi Li,*[,‡] Huajian Gao,*[,∥] and Xiaoyan Li*[,†]

[†]Center for Advanced Mechanics and Materials, Applied Mechanics Laboratory, Department of Engineering Mechanics, Tsinghua University, Beijing 100084, China

[‡]Shenyang National Laboratory for Materials Science, Institute of Metal Research, Chinese Academy of Sciences, Shenyang 110016, China

[§]State Key Laboratory of Structural Analysis for Industrial Equipment, Department of Engineering Mechanics, Dalian University of Technology, Dalian 116024, China

[∥]School of Engineering, Brown University, Providence, Rhode Island 02912, United States

Supporting Information

ABSTRACT: Mechanical metamaterials with three-dimensional micro- and nanoarchitectures exhibit unique mechanical properties, such as high specific modulus, specific strength, and energy absorption. However, a conflict exists between strength and recoverability in nearly all the mechanical metamaterials reported recently, in particular the architected micro/nanolattices, which restricts the applications of these materials in energy storage/absorption and mechanical actuation. Here, we demonstrated the fabrication of three-dimensional architected composite nanolattices that overcome the strength−recoverability trade-off. The nanolattices under study are made up of a high-entropy alloy-coated (14.2−126.1 nm in thickness) polymer strut (approximately 260 nm in the characteristic size) fabricated via two-photon lithography and magnetron sputtering deposition. In situ uniaxial compression inside a scanning electron microscope showed that these composite nanolattices exhibit a high specific strength of 0.027 MPa/kg m^3, an ultrahigh energy absorption per unit volume of 4.0 MJ/m^3, and nearly complete recovery after compression under strains exceeding 50%, thus overcoming the traditional strength−recoverability trade-off. During multiple compression cycles, the composite nanolattices exhibit a high energy loss coefficient (converged value after multiple cycles) of 0.5−0.6 at a compressive strain beyond 50%, surpassing the coefficients of all the micro/nanolattices fabricated recently. Our experiments also revealed that, for a given unit cell size, the composite nanolattices coated with a high entropy alloy with thickness in the range of 14−50 nm have the optimal specific modulus, specific strength, and energy absorption per unit volume, which is related to a transition of the dominant deformation mechanism from local buckling to brittle fracture of the struts.

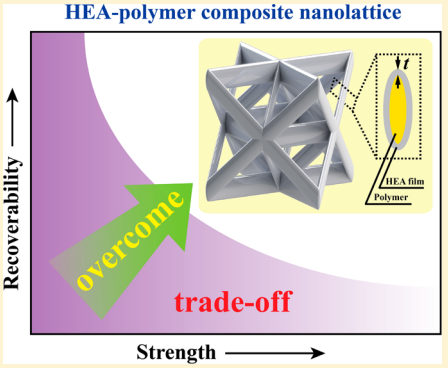

KEYWORDS: *nanolattice, high-entropy alloy-polymer composite, strength, recoverability*

Recent advances in additive manufacturing and processing techniques have led to the creation of mechanical metamaterials,[1−3] prominent examples including three-dimensional (3D) architected micro- and nanolattices that exhibit unusual mechanical properties and performances, e.g., negative Poisson's ratio, negative effective modulus, negative effective mass density, negative refraction index, and pentamode structure.[1,2] The mechanical properties of metamaterials can be tuned by tailoring the geometric parameters of their unit cell and/or basic structural elements.[3] During the past few years, tremendous experimental and modeling efforts have been dedicated to designing and fabricating mechanical metamaterials with optimized properties based on various 3D architectures and constituent materials, such as polymers,[4,5] metals,[4,6−10] ceramics,[11−14] and glassy carbon.[15] Remarkably, as the characteristic size of their building blocks is reduced to several hundred nanometers, the metamaterials possess a high specific modulus and specific strength (i.e., the ratios of modulus and yield strength over density),[4,9,15] giving these materials potential for applications in lightweight structures and devices.

As a novel type of cellular material, metamaterials have a broad range of applications, including lightweight structural components, energy absorption and storage, thermal insulation, electrochemical devices, catalyst supports, and tissue scaffolds.[1,2] The safety, reliability, and durability of metamaterials in these applications are mainly determined by their strength and recoverability. The yield strength, σ_y, scales with

Received: March 27, 2018
Revised: June 9, 2018
Published: June 14, 2018

DOI: 10.1021/acs.nanolett.8b01241
Nano Lett. 2018, 18, 4247−4256

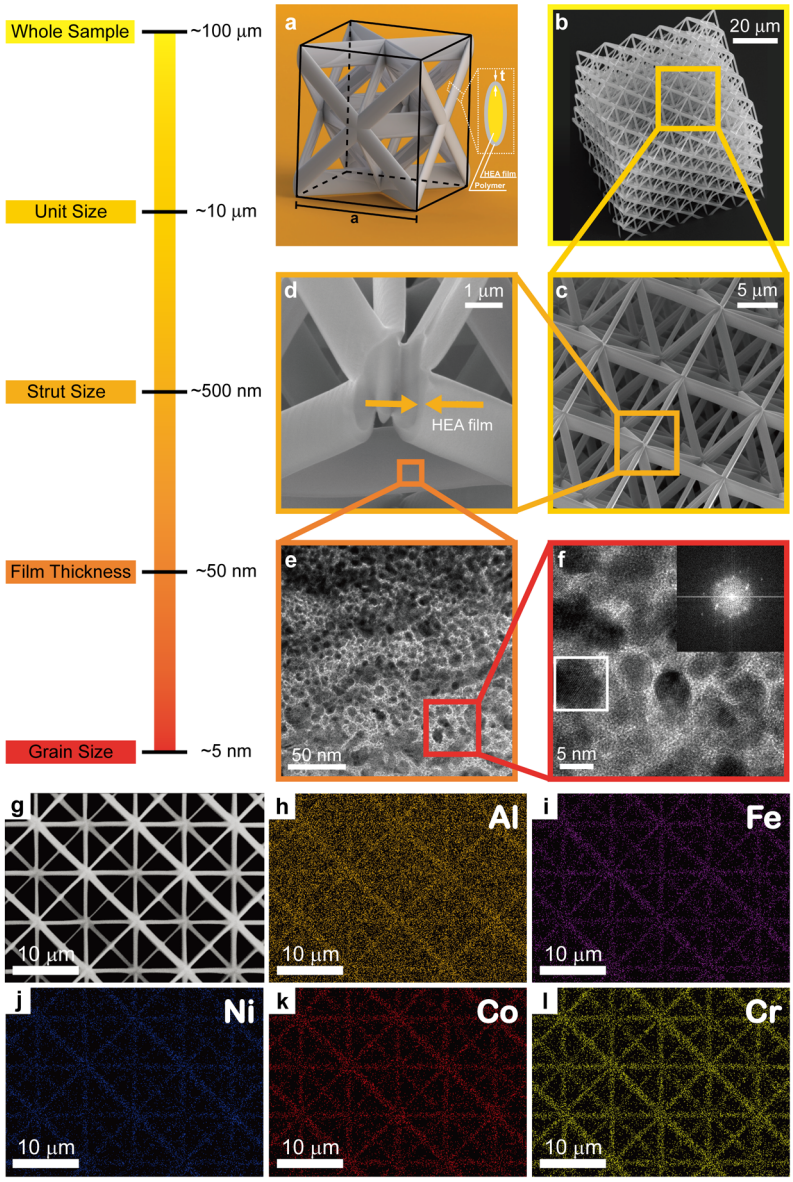

Figure 1. Structure of an HEA–polymer composite nanolattice across five orders of magnitude in length scale from the size of the whole sample (approximately 100 μm) to the grain size (approximately 5 nm) of the HEA coating. (a) Schematic illustration of the octet-truss unit cell with the characteristic sizes a (unit cell size) and t (thickness of HEA coating). (b) SEM image of a representative composite octet-truss nanolattice. (c,d) Magnified sections of the composite nanolattice. (e,f) HRTEM image of the nanocrystalline HEA coating. The inset in (f) is a fast Fourier transform (FFT) image of the nanocrystal marked by the solid line in (f). (g) Top view of the composite nanolattice. (h–l) EDS maps of the five metallic elements over the area shown in (g).

the density, ρ, in the relation $\sigma_y/\sigma_{ys} \sim (\rho/\rho_s)^n$, σ_{ys} and ρ_s being the yield strength and density of the constituent materials,[16] respectively. The exponent n depends on the architecture of the metamaterial and is generally larger than 1. This relationship between the strength and density suggests that the strength decreases significantly with a reduction in density. The recoverability reflects the ability of a material to recover its initial configuration after being subjected to a large applied strain in the plastic or inelastic regime. Generally, the recoverability of cellular materials is inversely related to the density; i.e., the lower the density, the higher the recoverability. For example, nearly all aerogels have an ultralow density <10 kg/m^3, leading to excellent recoverability even after compressive strains exceeding 50%.[17,18] These behaviors imply that the strength and recoverability of metamaterials are mutually exclusive. For quantification, here, we define the recoverability, r, as the ratio of the recovered strain, ε_r, to the total applied strain, ε_t, i.e., $r = \varepsilon_r/\varepsilon_t$. For a given strain, the recoverability of a material is close to zero if the material fractures and the recovered strain is very small.

Recently, micro/nanolattices with various controlled geometries have been fabricated via advanced processing techniques. The experimental measurement of their mechanical properties revealed a strength–recoverability trade-off in metamaterials. For example, metallic microlattices[6] with an octahedral array of hollow nickel-alloy tubes exhibit an ultralow density of approximately 0.9 kg/m^3 and completely recover after compression to a strain above 50%, indicating that r = 1. However, the strength of these microlattices with hollow nickel-alloy tubes[6] is only approximately 10 kPa. Glassy carbon

DOI: 10.1021/acs.nanolett.8b01241
Nano Lett. 2018, 18, 4247–4256

nanolattices[15] with a honeycomb topology have an ultrahigh strength of 1.2 GPa at a density of 600 kg/m^3 due to size-dependent strengthening effects. However, when the compressive strain reaches approximately 10%, these nanolattices exhibit catastrophic brittle fracture, leading to a recoverability of $r = 0$ at $\varepsilon_t > 10\%$.[15] Most recently, multiscale nickel-alloy microlattices with fractal configurations showed a recoverability of $r = 0.8$ at $\varepsilon_t = 20\%$ at a density of approximately 210 kg/m^3. However, the strength of these nanolattices[9] was as low as 80 kPa. Ceramic nanolattices composed of an octet network of hollow alumina tubes[12] exhibit a transition from ductile-like to brittle fracture as their density increases from 6 to 250 kg/m^3. When the density falls below 60 kg/m^3, these ceramic nanolattices have a maximum strength of 1.0 MPa and can recover the original shape after compression to approximately 40% strain, i.e., $r = 1$ at $\varepsilon_t = 40\%$.[12] Otherwise, the nanolattices collapse due to the brittle fracture of the tube wall when the compressive strain is beyond 5−10%, i.e., $r = 0$ at $\varepsilon_t > 10\%$.[12] In this case, the strength of the hollow ceramic nanolattices is in the range of 4−30 MPa. Notably, a polymer microlattice coated with a 800 nm-thick high-entropy-alloy (HEA) layer exhibited a density of 380 kg/m^3 and strength of 6.9 MPa;[19] however its fracture strain is only 6.5% under compression, suggesting $r = 0$ at $\varepsilon_t > 7\%$.[19]

The observed strength−recoverability trade-off in metamaterials might be related to the widely observed conflict between strength and ductility due to competitions between the strengthening and toughening mechanisms in materials.[20] Evading such trade-off to optimize properties (including strength, recoverability, and energy absorption) is vital for mechanical metamaterials. Nearly all metamaterials reported so far exhibit strength−recoverability trade-off, which might be because they are made of a single constituent material. Here, we create an octet-truss composite nanolattice made of two constituent materials, a polymer core and a HEA coating whose thickness varies from tens to hundreds of nanometers. The light and ductile polymer core serves as a frame for allowing the whole structure to recover after large deformation, while the ultrastrong HEA coating improves the strength. We will show that such polymer−HEA composite nanolattices simultaneously achieve high strength and good recoverability, thereby overcoming the strength−recoverability trade-off. During compression to a strain of 50%, the maximum strength of the composite nanolattice reaches 11.6 MPa, leading to an energy absorption per unit volume of 4.0 MJ/m^3, which is higher than that of most natural materials (such as bone, antler, and calcite) and micro/nanolattices reported previously.

The composite nanolattices were first fabricated from a polymer scaffold via two-photon lithography direct laser writing followed by coating the scaffold conformally with HEA films using magnetron sputtering deposition. More details of the fabrication method are given in Methods. The fabricated nanolattices were designed to have a periodic and repeated arrangement of an octet-truss unit cell, as illustrated in Figure 1a. The cross-section of each polymer strut is elliptical, with major- and minor-axis semilengths of 774.5 and 262.4 nm, respectively. During fabrication of the nanolattice, two design parameters were tuned to achieve the optimal properties: one is the unit cell size, a, which ranged from 8 to 15 μm, and the other is the HEA coating thickness, t, which was varied from 14.2 to 126.1 nm. Determination of HEA coating thickness is given in Methods. Figure 1b shows a scanning electron microscopy (SEM) image of the synthesized composite nanolattice with $a = 15$ μm and $t = 94.3$ nm. Figure 1c,d shows magnified sections of the composite nanolattice, revealing the elliptical cross-section of each strut. The SEM image provided in Figure 1d was taken of a node on the facet of a specimen cut by a focused ion beam (FIB) (see Figure S1a). During FIB milling, some of the polymer core near the cutting edge burned, leaving only the HEA film with a uniform thickness of approximately 90 nm (Figure S1d). This indicates that the HEA coating is conformal and that its thickness is consistent with the sputtering target thickness. More detailed examinations on the coating thickness are given in Supplementary Text 1. Parts of the nanolattice (Figure S4) were extracted and used for transmission electron microscopy (TEM) analysis. Figure 1e shows a TEM image of the coated HEA film, which contains a large number of nanosized grains. The average grain size of the HEA film is approximately 5 nm, as shown in the high-resolution TEM (HRTEM) image provided in Figure 1f. The length scale of the whole composite nanolattice structure spans five orders of magnitude, from several nanometers to hundreds of microns, as shown by the scale bar in Figure 1.

Unlike conventional alloys, HEAs generally contain five or more principle elements, with the atomic concentration of each element ranging from 5% to 35%.[21] HEAs exhibit high configurational entropy, severe lattice distortion, sluggish diffusion, and cocktail effects.[21] As a result, HEAs can achieve excellent mechanical properties, including high strength, good ductility, and exceptional fracture toughness, as well as good resistance to wear, corrosion, and oxidation.[21] In this work, the composition of the coated HEA film is $Al_{19.5}Cr_{19.9}Fe_{15.1}Co_{23.7}Ni_{21.9}$. Figure 1h−l shows SEM-energy dispersive spectroscopy (EDS) maps of the five metallic elements in the area of a representative composite nanolattice shown in Figure 1g, indicating a homogeneous elemental distribution in the nanolattice. The distributions of other elements (including C, O, and Si) are shown in Figure S5. During sputtering of the nanolattice, we simultaneously sputter-deposited HEA films on silicon and sapphire wafers in the same vacuum chamber. These as-deposited HEA films have nearly the same thickness as the HEA coating on the nanolattice and were used to further characterize the microstructures, phase, and mechanical properties of the HEA coating. X-ray diffraction (XRD) analysis (Figure S6) indicates that the HEA film contains body-centered-cubic (BCC) phases. TEM images of HEA films with different thicknesses are shown in Figure S7a−h. The mean grain size of these HEA films is approximately 5 nm, which is consistent with that of the HEA coating on the nanolattice. We measured the hardness of HEA films with thicknesses from 94.3 to 208.5 nm via nanoindentation. For a given indentation depth normalized by the film thickness, the hardness, H, of the HEA film is strongly dependent on the film thickness, t, and increases with decreasing film thickness (Figure S8), implying size-dependent hardness and strength. By tailoring the design parameters and utilizing such HEA films with a size-dependent hardness, a wide variety of materials with unprecedented properties can be created, including a strong, recoverable, and lightweight metamaterial in this study. Furthermore, based on the dimensions of the nanolattices measured by SEM and the densities of the polymer and HEA film, we estimated the absolute density, ρ, and relative density, $\bar{\rho}$, of the composite nanolattice to be 87.14−865.13 kg/m^3 and 0.056−0.234, respectively. All of the fabricated composite nanolattices have

DOI: 10.1021/acs.nanolett.8b01241
Nano Lett. 2018, 18, 4247−4256

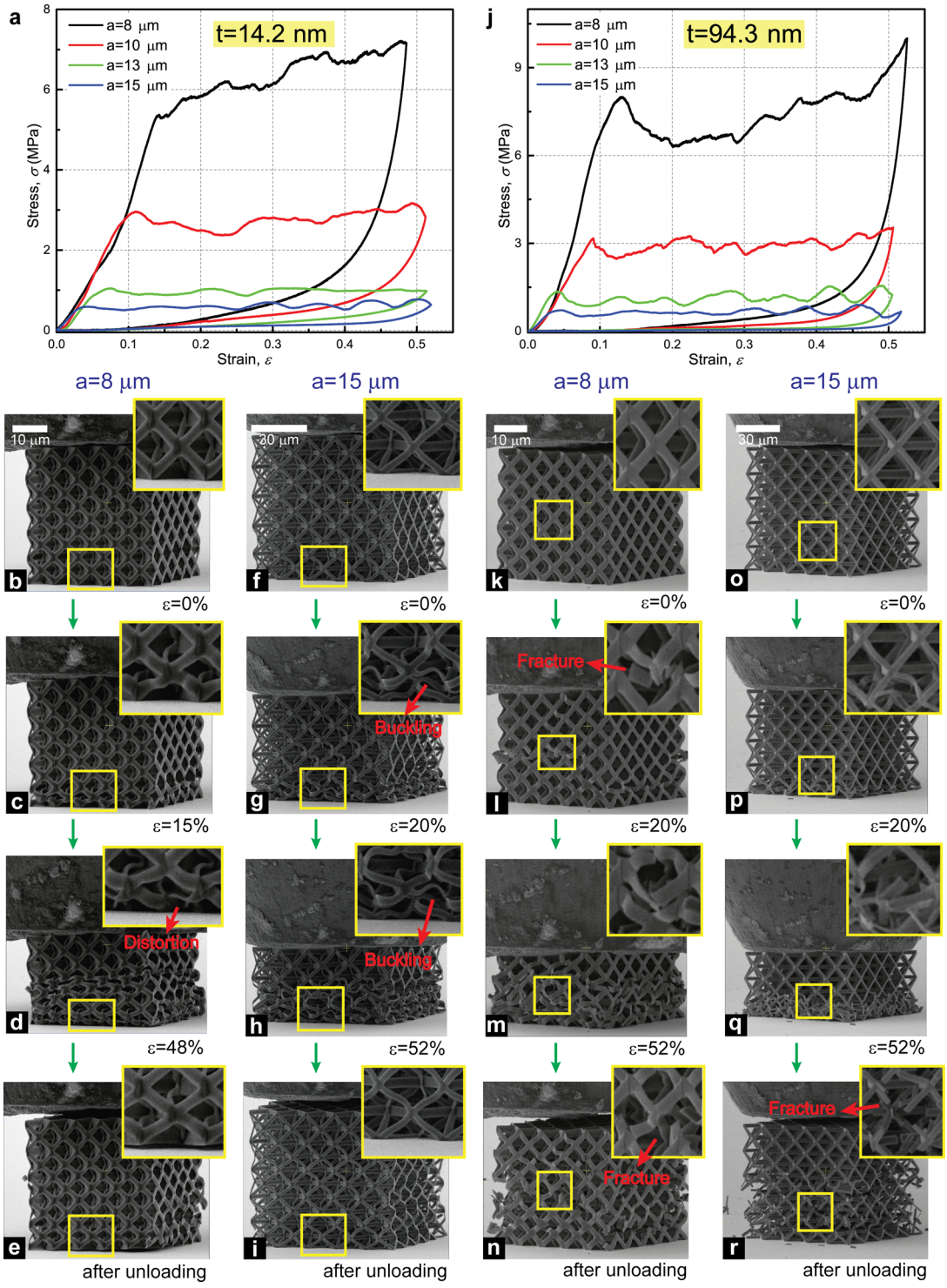

Figure 2. In situ uniaxial compression tests of composite nanolattices. (a) Stress–strain curves of nanolattices with a = 8–15 μm and t = 14.2 nm. (b–e) SEM images of a nanolattice with a = 8 μm and t = 14.2 nm during compression. (f–i) SEM images of a nanolattice with a = 15 μm and t = 14.2 nm during compression. The insets in (b–i) show the locally deformed structures, indicating local buckling of the struts during compression and nearly complete recovery after unloading. (j) Stress–strain curves of nanolattices with a = 8–15 μm and t = 94.3 nm. (k–n) SEM images of a nanolattice with a = 8 μm and t = 94.3 nm during compression. (o–r) SEM images of a nanolattice with a = 15 μm and t = 94.3 nm during compression. The insets in (k–r) show the locally deformed structures, indicating fracture of the struts.

densities below 1000 kg/m^3, indicating that they are lightweight structures.[22] Details of the density calculation can be found in Methods.

We performed in situ SEM compression tests on all fabricated polymer–HEA composite nanolattices. Figure 2a shows a series of stress–strain curves for the composite nanolattices with a = 8–15 μm and t = 14.2 nm. After an initial linear elastic stage, a plastic-like plateau occurs in nearly all stress–strain curves, corresponding to the yielding of the composite nanolattices. Upon unloading, all the nanolattices

DOI: 10.1021/acs.nanolett.8b01241
Nano Lett. 2018, 18, 4247–4256

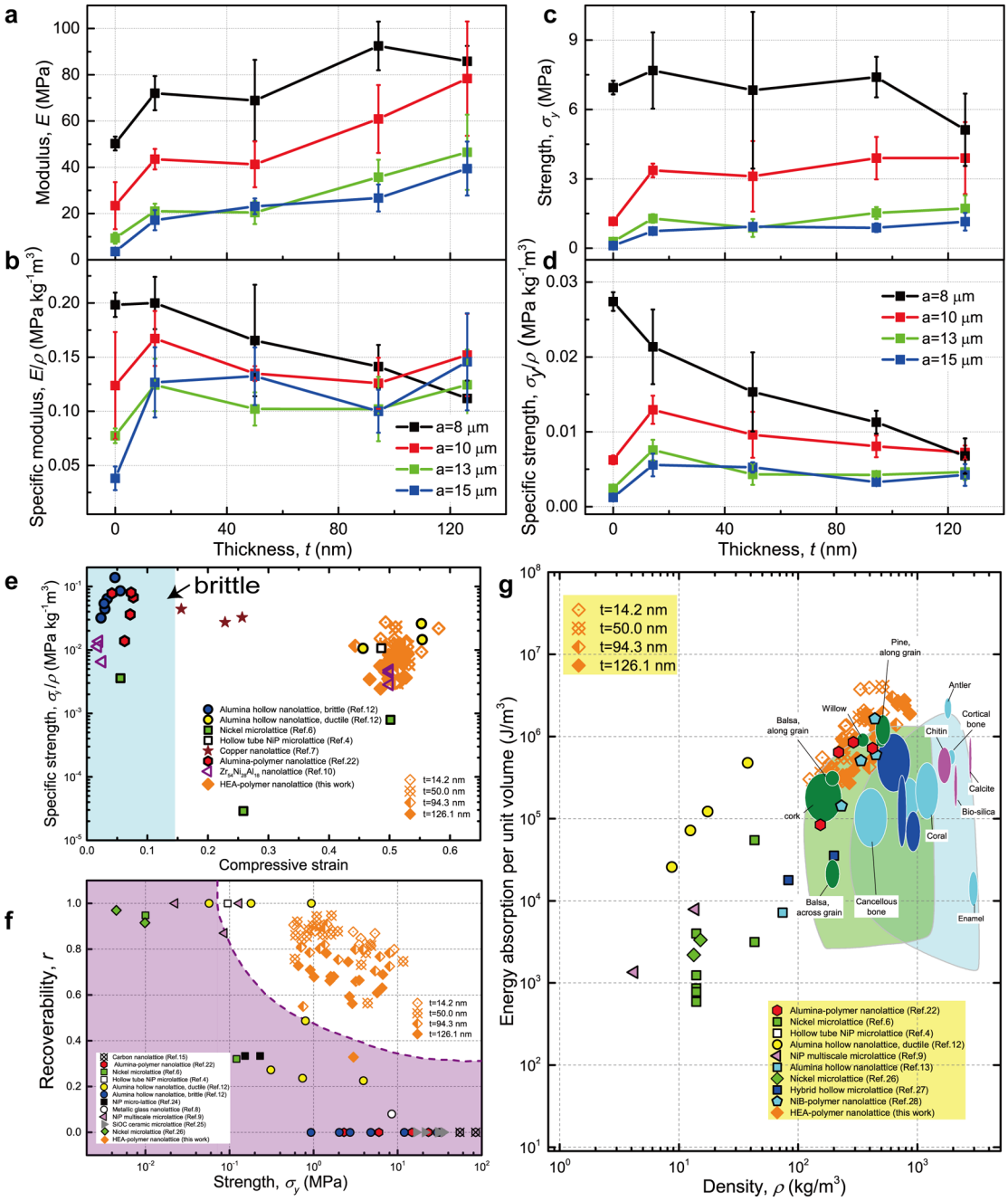

Figure 3. Mechanical properties of HEA−polymer composite nanolattices. (a−d) Variations of modulus, specific modulus, strength, and specific strength with thickness of the HEA coating. (e) Specific strength versus compressive strain for our composite nanolattices and other lattices reported recently. For all materials in the brittle regime and copper nanolattices, the compressive strain in (e) corresponds to the strain at failure. For the other lattices, the compressive strain in (e) reflects the maximum applied strain in the corresponding experiments. (f) Recoverability versus strength for our composite nanolattices and other lattices reported recently. (g) Ashby map of energy absorption per unit volume versus density. This chart compares our composite nanolattices against other architected lattices reported so far and against natural cellular materials.

almost completely recover. Figure 2b−e depicts a series of SEM images of the deformed nanolattices during compression. During the initial stage of yielding, the struts near the bottom buckle first (Figure 2c). As the compressive strain increases, the buckled struts undergo severe deformation. For example, some struts are heavily distorted and even make partial contact with other buckled struts (Figure 2d,h). Throughout compression, severe buckling propagates from the bottom to the top like a wave, leading to gradual densification of the structure. The elastic buckling allows for extensive rotation/distortion around the thin struts without introducing plastic strain, leading to nearly complete recovery even after a compressive strain exceeds 50%. Similar phenomena are observed in Figure 2f−i and Movies S1 and S2. Figure 2j shows stress−strain curves of the composite nanolattices with a = 8−15 μm and t = 94.3 nm. In contrast to the stress−strain curves shown in Figure 2a, the stress in the curves shown in Figure 2j apparently drops after the initial yielding. Such a stress drop can be attributed to fracture in some of the struts. As compression continues, more struts fracture, leading to permanent damage of the nanolattice. While fracture is usually initiated at the nodes due to stress concentration (insets in

DOI: 10.1021/acs.nanolett.8b01241
Nano Lett. 2018, 18, 4247−4256

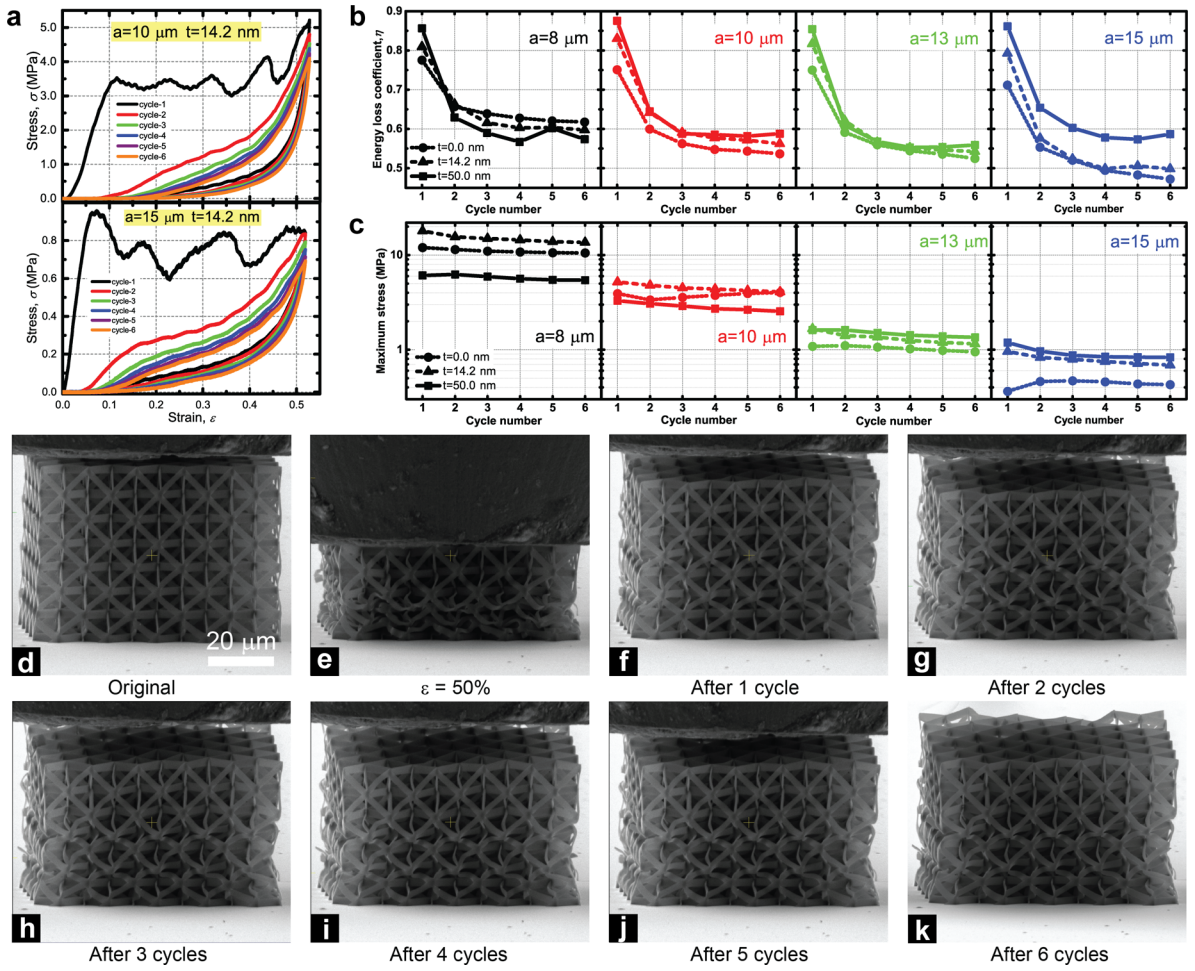

Figure 4. Multiple compression cycles of HEA−polymer composite nanolattices. (a) Cyclic stress−strain curves of composite nanolattices with a = 10 and 15 μm and t = 14.2 nm. (b,c) Variations in energy loss coefficient and maximum stress with cycle number in composite nanolattices with a = 8−15 μm and t = 0−50.0 nm. (d−k) Series of SEM images of deformed nanolattices during multiple compression cycles.

Figure 2m,n), it is typically localized in a certain region and does not lead to catastrophic failure of the whole nanolattice. During compression, some struts still undergo large deformation via elastic buckling. Thus, the nanolattice can partially recover after unloading. These phenomena are observed in Movies S3 and S4. We summarized the variation in the recovered strain of all the nanolattices with changing HEA coating thicknesses in Figure S9a. The data show that for a given unit cell size the recovered strain after unloading generally decreases with increasing HEA coating thickness, as exemplified by Figure S9b. The reason for this is that as the coating thickness increases, the dominant deformation mechanism transitions from local buckling to brittle fracture of the struts. Our experimental observations show that when the coating thickness rises above 50 nm, fracture around the nodes becomes the controlling mechanism; otherwise, local buckling dominates throughout compression. We also observed from Figure S9a that, for a specific coating thickness, nanolattices with larger unit cells exhibit larger recovered strains and better recoverability. This may be attributed to the fact that the local buckling of struts preferentially occurs in nanolattices with large unit cells.

We further investigated the influence of two design parameters in optimizing the mechanical properties (Young's modulus, yield strength, specific modulus, specific strength, recoverability, and energy absorption per unit volume) of the composite nanolattice. We extracted both Young's modulus E and yield strength σ_y from the stress−strain curves from the in situ uniaxial compression tests, E by fitting the linear elastic portion of the stress−strain curve, and σ_y as the first stress peak at the initial yield. Figure 3a−d shows the modulus, specific modulus (i.e., the ratio of modulus over density), strength, and specific strength (i.e., the ratio of strength over density), respectively, as functions of the HEA coating thickness, t. Each data point in these figures is the average from experimental measurements on 3−5 specimens. The error bars reflect the standard deviation. The large error is primarily due to structural imperfections introduced during fabrication and the resultant localized deformation. The measured modulus nearly monotonically increases with increasing coating thickness, as shown in Figure 3a, improving up to an order of magnitude over that of the pure polymer nanolattice (i.e., t = 0 nm). As the coating thickness increases, the strength first dramatically increases and then gradually saturates. The initial increase is due to the introduction of the HEA film with a much higher yield strength than that of the polymer, while the subsequent saturation is attributed to the dominance of localized deformation during compression and the size effect on strength of the HEA film (i.e., its strength increases with decreasing film thickness). The strength of the tested

DOI: 10.1021/acs.nanolett.8b01241
Nano Lett. 2018, 18, 4247−4256

composite nanolattices is up to an order of magnitude higher than that of the pure polymer nanolattice (i.e., t = 0 nm). Because of the superior strength imparted by the nanoscale HEA film, our composite nanolattices are superior to the commercially available metallic foams with comparable densities. At a density of approximately 690 kg/m^3, our composite nanolattice has a compressive strength of approximately 8.03 MPa, whereas a nickel foam with the same density has a strength of 2.57 MPa.[23] Notably, both the specific modulus and specific strength of the composite nanolattice increase once the thin HEA film is deposited, as the modulus and strength of HEA are much higher than those of the polymer. However, as the coating thickness increases, both the specific modulus and specific strength slightly decrease. This result indicates a nonmonotonic dependence of these two properties on the coating thickness. As shown in Figure 3b,d, for a given unit cell size, the composite nanolattices with coating thicknesses of 14.2−50.0 nm have the optimal specific modulus and specific strength.

We compared the compressive properties of our HEA−polymer nanolattices with those of other recently reported lightweight micro/nanolattices.[4,6−10,12,13,15,22,24−28] As shown in Figure 3e, for both the specific strength and maximum compressive strain, our composite nanolattices outperform all the other reported lightweight micro/nanolattices. Figure 3f shows the recoverability versus strength of our composite nanolattices and the other lattices reported to date. For nearly all the previous micro/nanolattices, the strength and recoverability are mutually exclusive. However, our HEA−polymer nanolattices exhibit a superior combination of good recoverability and high strength (Figure 3f). This is partly attributed to the fact that our nanolattice is made from the HEA−polymer composite. The light and soft polymer core enables the whole structure to recover after large deformation, while the ultrastrong HEA coating improves both modulus and strength. These results suggest that using a composite to construct metamaterials provides an efficient route to overcoming the strength−recoverability trade-off. As the HEA coating thickness increases from 14.2 nm, the strength enhancement nearly saturates due to the occurrence of local buckling or fracture around the nodes during the initial stage of deformation. This implies that improving the nodal strength and suppressing local deformation will be critical for further enhancing the strength of the composite nanolattices. Due to their high strength and large compressive strain, our composite nanolattices have an ultrahigh energy absorption per unit volume of 4.0 MJ/m^3 (Figure 3g). The energy absorption per unit volume was calculated by integrating the area under the loading−unloading stress−strain curve. As shown in Figure 3g, the energy absorption per unit volume of our composite nanolattice is 1−3 orders of magnitude larger than that of some natural porous materials with comparable densities. If the relationship between the energy absorption and density follows a scaling law, our HEA−polymer nanolattices have a larger scaling exponent than most of the recoverable micro/nanolattices reported recently.[4,6,9,12,15,22,25−27] This observation implies that our nanolattices have higher energy absorptions than other micro/nanolattices with comparable densities.

We further performed a series of cyclic loadings on our nanolattices with a = 8−15 μm and t = 0−50.0 nm. During compression, the nanolattices exhibit good recoverability after compression to above 50% strain. Figure 4a shows two typical cyclic stress−strain curves of the composite nanolattices with a = 10 and 15 μm and t = 14.2 nm. In the first cycle of both stress−strain curves, the linear elastic stage is followed by a yield plateau due to local buckling or fracture around the nodes. For the nanolattices with smaller unit cells, hardening occurs due to densification near the end of the compression stage. However, the yield plateau is absent in the second cycle, and the maximum stress is always achieved at the end of compression. The stress−strain curves in the subsequent cycles are nearly identical to that in the second cycle. We summarized the evolution of the energy loss coefficient and maximum stress with increasing cycle number. The energy loss coefficient is the ratio of dissipated energy over the work done during compression and reflects the hysteresis of the material during cyclic deformation. The energy loss coefficient first decreases with increasing of cycle number, and then nearly converges to a constant after three cycles (Figure 4b). For all the tested samples, the converged energy loss coefficient is as high as 0.5−0.6, which is higher than those (highest value of 0.4) of recently reported micro/nanolattices[6,9,12,24] at compressive strains beyond 50%. Recent experimental studies on the fabrication of polymer and polymer−ceramic microlattices and their behaviors under cyclic loading[29] reported their energy loss coefficients in the ranges of 0.52−0.55 and 0.38−0.44, respectively,[29] which are comparable to those found in our composite nanolattices. However, previous reported values were obtained at a maximum compressive strain of only 28%,[29] which is smaller than that of 50% for our composite nanolattices. The maximum stress level remains almost constant throughout cyclic deformation. In terms of both the energy loss coefficient and the maximum stress, nearly all the composite nanolattices with HEA coatings are superior to the pure polymer nanolattice, indicating that the HEA coating plays a very important role in improving the stress and hysteresis (energy absorption) during cyclic deformation. Figure S10a,b shows the variations of energy absorption per unit volume and recoverability with the cycle number in composite nanolattices with a = 8−15 μm and t = 0.0−50.0 nm, respectively. In each cycle, the composite nanolattices with t = 14.2 nm always exhibit higher energy absorption per unit volume than the corresponding pure polymer nanolattices (Figure S10a). However, the composite nanolattices have lower recoverability than the polymer nanolattices, implying that the HEA coating improves energy dissipation at a sacrifice of recoverability. It is noted that, as the unit cell size increases, the recoverability of all nanolattices during cyclic loading increases. When the unit cell size is up to 13−15 μm, the recoverability of the composite nanolattices is close to those of the polymer nanolattices. Figure 4d−k shows a series of SEM snapshots of the composite nanolattice with a = 15 μm and t = 14.2 nm during cyclic compression. We observed that, after the first cycle, the nanolattice recovers 93% of its original height (Figure 4f). In the second cycle, discrete localized fracture events lead to gradual damage of the structure. As the cycle number increases, the damage accumulation causes the residual strain of the nanolattice to gradually increase. After the sixth cycle, the nanolattice still recovers 85% of its original height (Figure 4k). Notably, the whole nanolattice does not exhibit catastrophic failure throughout cyclic compression, showing substantial damage tolerance of the structure.

Recent experimental studies[30−33] reported the deposition of various metals and alloys to polymer micro/nanolattices via magnetron sputtering. These experimental studies showed that

DOI: 10.1021/acs.nanolett.8b01241
Nano Lett. 2018, 18, 4247−4256

the coating thickness viewed from the cross-sections of struts pronouncedly varies from the top to bottom or from the outermost to innermost regions of micro/nanolattice samples. In contrast to the previously studies,[30−33] our nanolattices exhibit more uniform coating thickness (Figures S1−S3). The reason can be partially attributed to different processing conditions and parameters of magnetron sputtering, including the relative location between the targets and samples and the sputtering rate. In previous studies,[30−33] only one target was used and placed vertically relative to the samples, the sputtering rate was up to about 10 nm min^{-1}, and the sample was stationary or rotated relatively to the target with frequency up to about one round per min. The base pressure was about 1−4.5 × 10^{-6} Torr, and the processing pressure was 3−4 mTorr with pure Ar gas. In contrast, in our sputtering process, we used two targets: one was the Al target with a diameter of 5.08 cm, and the other was the FeNiCoCr target with a diameter of 5.08 cm. The relative location between the targets and the sample, as shown in Figure S11, differs from that in previous experiments. Our sputtering rate of less than 5 nm min^{-1} was also lower than those used in previous experiments. The sample rotated at a frequency of 10 rounds min^{-1}, which is faster than those used in previous experiments. The base pressure was about 0.75 × 10^{-7} Torr, and the processing pressure was 2.25 mTorr in pure Ar gas. These conditions and parameters led to more uniform coating thickness in our nanolattices compared to previous studies.[30−33] Moreover, the micro/nanolattices from previous studies[30−33] have circular or rounded square cross-sections, while our nanolattices have an elliptical cross-section. When metals or alloys are sputtered from the targets down to the samples, the coating near the top is somewhat thicker than that near the bottom, as shown from a cross-section view in Figure S12. For the elliptical cross-section, the nonuniformity in coating thickness seems less pronounced, compared with the circular or rounded square cross-sections. In this sense, the elliptical cross-section may have also facilitated the uniformity in coating thickness to some extent.

Previous experiments[22] reported the fabrication of microlattices with polymer cores and ceramic coatings using direct laser writing and atomic layer deposition. The ceramic−polymer microlattices have a maximum strength of approximately 30 MPa (which is comparable to the strength of our nanolattice of approximately 10 MPa), but they always fail via brittle fracture at a compressive strain of only 4%. The reason is that the ceramic coating is intrinsically brittle. The size of the struts in the ceramic−polymer microlattice is approximately 1 μm, which is about twice that (approximately 520 nm) of our HEA−polymer nanolattices. In addition to the difference in the feature size, our nanolattice utilizes ductile HEA, which can undergo much larger plastic deformation than the brittle ceramics. Due to the nanoscale feature size and the metallic composite, our HEA−polymer nanolattices have a better recoverability and damage tolerance at larger compressive strains than the ceramic−polymer microlattices but without substantial degradation of the strength. Recent experiments demonstrated the fabrication of hollow microlattices with a sandwich wall architecture containing an elastomeric core and metallic skins via a scalable additive manufacturing process.[27] Such hybrid hollow microlattices exhibited a combination of high damping, high stiffness, and good recoverability under large compressive strain.[27] The underlying deformation mechanism is dominated by local buckling of hollow struts, which is similar to that observed in our composite nanolattices with thinner HEA coatings. In these hybrid microlattices, the elastomeric cores contribute to the damping and recoverability, while the metallic skins provide the stiffness and strength.[27] Our current results, together with those on ceramic−polymer[22] or metallic−polymer microlattices,[27] indicate that the fabricated composite micro/nanolattices is an effective strategy to achieve a combination of good mechanical properties and performances.

In summary, we have fabricated novel HEA−polymer composite octet-truss nanolattices with a unit cell size of a = 8−15 μm and an HEA coating thickness of t = 14.2−126.1 nm. In situ compression tests revealed that such composite nanolattices exhibit a combination of high specific strength, ultrahigh energy absorption per unit volume, high energy loss coefficient, and excellent recoverability under compression to strains exceeding 50%, overcoming the strength−recoverability trade-off exhibited by the mechanical metamaterials reported previously. Our experimental results also provided an optimized design for the composite nanolattice; i.e., for a given unit cell size, the nanolattices with t = 14.2−50.0 nm achieved the optimal properties. This optimized design is associated with the dependence of the local deformation mode (buckling or fracture around the nodes) during compression on the coating thickness. Our results create an avenue for fabricating and designing composite mechanical metamaterials with unique mechanical properties that are probably inaccessible to metamaterials made of a single-constituent material and provide a fundamental understanding of the relationships between the geometry, mechanical properties, and deformation mechanisms in composite metamaterials.

Methods. *Fabrication of Composite Nanolattice.* We fabricated HEA−polymer composite nanolattices by using two-photon lithography direct laser writing (Nanoscribe) and magnetron sputtering deposition. Frist, the polymer octet-truss nanolattice was printed through direct laser writing process via IP-L photoresist with laser power of 112.5 mW and writing speed of 24 μm s^{-1}. Then these polymer nanolattices were conformally coated by HEA films via magnetron sputtering deposition. HEA films were deposited on the polymer nanolattice structures in an ultrahigh-vacuum deposition system via cosputtering of elemental Al target (99.999% purity) and equi-atomic FeNiCoCr alloy target (99.9% purity). Figure S11 shows a schematic illustration of deposition HEA to polymer nanolattices via magnetron sputtering. For the Al target, a radiofrequency generator was employed, while for the FeNiCoCr target, a direct current magnetron was utilized. The base pressure was lower than 0.75 × 10^{-7} Torr, and the processing pressure was 2.25 mTorr using pure Ar gas. The power densities were 1.1 and 0.9 W/cm^2 for the Al and FeNiCoCr target, respectively. The substrate rotated at a frequency of 10 rounds min^{-1} to guarantee homogeneous film distribution. The film grew at a rate of 5 nm min^{-1}. During sputtering, a real-time temperature monitoring system was placed in the sputtering chamber to track the variation of temperature. The measured temperature during sputtering was around 30 °C, which does not significantly induce cross-linking of the polymer.

In Situ SEM Compressive Testing. We performed in situ SEM uniaxial compression tests on all fabricated nanolattices using a plat punch diamond tip with a diameter of 100 μm (PI 85, Hysitron). During loading, the nanolattice was compressed at a constant strain rate of 10^{-3} s^{-1}. Engineering stress−strain

DOI: 10.1021/acs.nanolett.8b01241
Nano Lett. 2018, 18, 4247−4256

curves were obtained by using recorded load−displacement data to separately divide by the nominal cross-sectional area and the height of the whole nanolattice.

As-Deposited HEA Film and Measurement of HEA Coating Thickness. During sputtering of the nanolattice, we simultaneously sputter-deposited HEA films on silicon and sapphire wafers in the same vacuum chamber. These as-deposited HEA films were used to measure the HEA coating thickness and further characterize the microstructures, phase, and mechanical properties of the HEA coating. To further verify the dependence of hardness of HEA films on the thickness, we also deposited the HEA films with thickness of 208.5 nm using the same method with the same processing parameters. We measured the thickness of the as-deposited HEA film using a step profiler and took the average over multiple measurements as thickness of the corresponding HEA coating of composite nanolattice. All composite nanolattices have four types of HEA coating thicknesses, including 14.2 ± 2.4, 50.0 ± 4.6, 94.3 ± 6.6, and 126.1 ± 6.8 nm.

Microstructural Characterization. The microstructural characterization of composite nanolattice was conducted using a SUPERA 55 scanning electron microscopy (SEM, LEO, Oberkochen, Germany) equipped with Oxford EDX and a 300 kV Tecnai G^2 F30 (FEI, Netherland) transmission electron microscope (TEM). Cross-sectional SEM and TEM analysis was extracted using a focused ion beam (FIB) workstation (Nova 200 NanoLab UHR FEG-SEM/FIB, Netherland). The chemical composition and structure of the simultaneously as-deposited thin films on the silicon and sapphire substrates were further determined with a Shimadzu EPMA-1610 equipped with a wavelength dispersive X-ray spectrometer (WDS) and a Rigaku D/max 2400 diffractometer with monochromated Cu Ka radiation (k = 0.1542 nm).

Nanoindentation Testing on HEA Films. To measure the modulus and hardness of HEA film, we performed a series on nanoindentation tests (TI 950 TriboIndenter, Hysitron) on HEA films with different thicknesses (94.3, 126.1, and 208.5 nm) sputtered on both silicon and sapphire substrates. During nanoindentation, a Berkovich indenter was used to measure the hardness of as-deposited HEA films. For each film, we tested four different indentation depths ranging from 20% to 80% of the film thickness. For each given depth, the hardnesses H of the as-deposited HEA films were obtained by averaging six measurement results. Figure S8 shows the average hardness of HEA films with different thicknesses on silicon and sapphire as a function of indentation depth normalized by the film thickness. For HEA films with thickness of 126.1 and 208.5 nm, their average hardness is nearly constant on both substrates under different indentation depths. However, for the HEA film with thickness of 94.3 nm, its average hardness first increases with increasing depth and then saturates to a constant. These results are consistent with previous experimental results reported in the literature.[34] It is noted that for a given indentation depth normalized by the film thickness, the hardness of the HEA film increases as the film thickness is reduced, indicative of an apparent size dependence in hardness and strength.

Estimation of Density of Nanolattices. The composition of HEA film was determined through WDS as $Al_{19.5}Cr_{19.9}Fe_{15.1}Co_{23.7}Ni_{21.9}$. According to the mixture of rule and the densities of individual elements (Table S1), the density ρ_a of the sputtered HEA film was estimated as 7200 kg/m^3. The density of liquid IP-L photoresist is 1170 kg/m^3. During the solidification of the liquid photoresist, its volume shrinkage is 1.40−15.83%. Considering such volume shrinkage, we estimated the density ρ_p of solid IP-L photoresist (i.e., polymer core in composite nanolattice) as 1280 kg/m^3. Using SEM measured dimensions of fabricated nanolattices, we constructed three-dimensional (3D) finite element models to investigate the effects of nodes, then estimated the total volume fractions of the polymer core and the HEA coating based on the models, and finally used their volume fractions and densities (i.e., ρ_p and ρ_a estimated above) to determine the density of the composite nanolattice via the following expression:

$$\rho = \frac{\rho_p V_p + \rho_a V_a}{V_p + V_a} \quad (1)$$

where V_p and V_a are the volumes of the polymer core and the HEA coating, respectively. The relative density is defined as the volume fraction of solid materials in the nanolattice and can be estimated based on the models. The absolute density ρ and relative density $\bar{\rho}$ of composite nanolattice vary from 87.14 to 865.13 kg/m^3 and from 0.056 to 0.234, respectively.

■ ASSOCIATED CONTENT

Supporting Information

The Supporting Information is available free of charge on the ACS Publications website at DOI: 10.1021/acs.nanolett.8b01241.

In situ compression of HEA-polymer composite nanolattice with a = 10 μm and t = 14.2 nm (AVI)
In situ compression of HEA-polymer composite nanolattice with a = 15 μm and t = 14.2 nm (AVI)
In situ compression of HEA-polymer composite nanolattice with a = 10 μm and t = 94.3 nm (AVI)
In situ compression of HEA-polymer composite nanolattice with a = 15 μm and t = 94.3 nm (AVI)
Examination of coating thickness of composite nanolattices. SEM images of composite nanolattice with coating thickness of 94.3 nm cut by FIB. SEM images of cross-sections of struts in composite nanolattices with HEA coating thickness of 126.1 and 14.2 nm. Sample (extracted by FIB) used for TEM observations. EDS mapping for distributions of carbon, oxygen, and silicon in nanolattice. XRD analysis on as-deposited HEA film. TEM images of as-deposited HEA films on silicon substrate. Dependence of the hardness of HEA films on film thickness and indentation depth. Recovered strain of composite nanolattices upon unloading. Energy absorption per unit volume and recoverability of composite nanolattices under cyclic compression. Schematic illustration of deposition HEA to polymer nanolattices via magnetron sputtering with two targets. Schematic illustration of HEA coating on struts with different cross-sections. Densities of five metallic elements in HEA film (PDF)

■ AUTHOR INFORMATION

Corresponding Authors

*E-mail: xiaoyanlithu@tsinghua.edu.cn.
*E-mail: jhyao@imr.ac.cn.
*E-mail: liyi@imr.ac.cn.
*E-mail: huajian_gao@brown.edu.

DOI: 10.1021/acs.nanolett.8b01241
Nano Lett. 2018, 18, 4247−4256

ORCID

Xiaoyan Li: 0000-0002-2953-9267

Author Contributions

X.L., Y.L., and H.G. designed the study. X.Z. and J.Y. fabricated the samples. X.Z. performed the mechanical testing. J.Y. conducted the microstructural characterization. X.Z., J.Y., X.L., and H.G. wrote the paper. All authors analyzed the data, discussed the results, and commented on the manuscript.

Notes

The authors declare no competing financial interest.

■ ACKNOWLEDGMENTS

The authors gratefully acknowledge financial support from the National Natural Science Foundation of China (Grant Nos. 11522218, 11720101002, 11372152, and 51420105001), the National Basic Research of China (Grant No. 2015CB932500), and the National Science Foundation (Grant No. DMR-1709318). X.L. also acknowledges support from the Chinese 1000-talents Plan for Young Researchers. We thank Jun Tan and Peng Wan at Institute of Metal Research for their help during FIB milling and TEM analysis.

■ REFERENCES

(1) Montemayor, L.; Chernow, V.; Greer, J. R. *MRS Bull.* **2015**, *40*, 1122−1129.
(2) Christensen, J.; Kadic, M.; Kraft, O.; Wegener, M. *MRS Commun.* **2015**, *5*, 453−462.
(3) Li, X.; Gao, H. *Nat. Mater.* **2016**, *15*, 373−374.
(4) Zheng, X.; Lee, H.; Weisgraber, T. H.; Shusteff, M.; DeOtte, J.; Duoss, E. B.; Kuntz, J. D.; Biener, M. M.; Ge, Q.; Jackson, J. A.; Kucheyev, S. O.; Fang, N. X.; Spadaccini, C. M. *Science* **2014**, *344*, 1373−1377.
(5) Meza, L. R.; Zelhofer, A. J.; Clarke, N.; Mateos, A. J.; Kochmann, D. M.; Greer, J. R. *Proc. Natl. Acad. Sci. U. S. A.* **2015**, *112*, 11502−11507.
(6) Schaedler, T. A.; Jacobsen, A. J.; Torrents, A.; Sorensen, A. E.; Lian, J.; Greer, J. R.; Valdevit, L.; Carter, W. B. *Science* **2011**, *334*, 962−965.
(7) Gu, X. W.; Greer, J. R. *Extreme Mech Lett.* **2015**, *2*, 7−14.
(8) Lee, S. W.; Jafary-Zadeh, M.; Chen, D. Z.; Zhang, Y.; Greer, J. R. *Nano Lett.* **2015**, *15*, 5673−5681.
(9) Zheng, X.; Smith, W.; Jackson, J.; Moran, B.; Cui, H.; Chen, D.; Ye, J.; Fang, N.; Rodriguez, N.; Weisgraber, T.; Spadaccini, C. M. *Nat. Mater.* **2016**, *15*, 1100−1106.
(10) Liontas, R.; Greer, J. R. *Acta Mater.* **2017**, *133*, 393−407.
(11) Jang, D.; Meza, L. R.; Greer, F.; Greer, J. R. *Nat. Mater.* **2014**, *12*, 893−898.
(12) Meza, L. R.; Das, S.; Greer, J. R. *Science* **2014**, *345*, 1322−1326.
(13) Meza, L. R.; Greer, J. R. *J. Mater. Sci.* **2014**, *49*, 2496−2508.
(14) Meza, L. R.; Phlipot, G. P.; Portela, C. M.; Maggi, A.; Montemayor, L. C.; Comella, A.; Kochmann, D. M.; Greer, J. R. *Acta Mater.* **2017**, *140*, 424−432.
(15) Bauer, J.; Schroer, A.; Schwaiger, R.; Kraft, O. *Nat. Mater.* **2016**, *15*, 438−443.
(16) Gibson, L. J., Ashby, M. F. *Cellular Solids: Structure and Properties*, 2nd ed.; Cambridge University Press: Cambridge, 1999.
(17) Zou, J.; Liu, J.; Karakoti, A. S.; Kumar, A.; Joung, D.; Li, Q.; Khondaker, S. I.; Seal, S.; Zhai, L. *ACS Nano* **2010**, *4*, 7293−7302.
(18) Qiu, L.; Liu, J. Z.; Chang, S. L.; Wu, Y.; Li, D. *Nat. Commun.* **2012**, *3*, 1241.
(19) Surjadi, J. U.; Gao, L.; Cao, K.; Fan, R.; Lu, Y. *Sci. Rep.* **2018**, *8*, 5442.
(20) Ritchie, R. O. *Nat. Mater.* **2011**, *10*, 817−822.
(21) Zhang, Y.; Zuo, T.; Tang, Z.; Gao, M. C.; Dahmen, K. A.; Liaw, P. K.; Lu, Z. *Prog. Mater. Sci.* **2014**, *61*, 1−93.
(22) Bauer, J.; Hengsbach, S.; Tesari, I.; Schwaiger, R.; Kraft, O. *Proc. Natl. Acad. Sci. U. S. A.* **2014**, *111*, 2453−2458.
(23) Queheillalt, D. T.; Katsumura, Y.; Wadley, H. N. G. *Scr. Mater.* **2004**, *50*, 313−317.
(24) Torrents, A.; Schaedler, T. A.; Jacobsen, A. J.; Carter, W. B.; Valdevit, L. *Acta Mater.* **2012**, *60*, 3511−3523.
(25) Eckel, Z. C.; Zhou, C.; Martin, J. H.; Jacobsen, A. J.; Carter, W. B.; Schaedler, T. A. *Science* **2016**, *351*, 58−62.
(26) Salari-Sharif, L.; Schaedler, T. A.; Valdevit, L. *J. Mater. Res.* **2014**, *29*, 1755−1770.
(27) Salari-Sharif, L.; Schaedler, T. A.; Valdevit, L. *J. Eng. Mater. Technol.* **2018**, *140*, 031003.
(28) Mieszala, M.; Hasegawa, M.; Guillonneau, G.; Bauer, J.; Raghavan, R.; Frantz, C.; Kraft, O.; Mischler, S.; Michler, J.; Philippe, L. *Small* **2017**, *13*, 1602514.
(29) Schroer, A.; Wheeler, J. M.; Schwaiger, R. *J. Mater. Res.* **2018**, *33*, 274−289.
(30) Montemayor, L. C.; Greer, J. R. *J. Appl. Mech.* **2015**, *82*, 071012.
(31) Liontas, R.; Greer, J. R. *Acta Mater.* **2017**, *133*, 393−407.
(32) Thompson, R. L.; Wang, Y.; Greer, J. R. *Adv. Eng. Mater.* **2018**, *20*, 1701055.
(33) Juarez, T.; Schroer, A.; Schwaiger, R.; Hodge, A. M. *Mater. Des.* **2018**, *140*, 442−450.
(34) Saha, R.; Nix, W. D. *Acta Mater.* **2002**, *50*, 23−38.

DOI: 10.1021/acs.nanolett.8b01241
Nano Lett. 2018, 18, 4247−4256